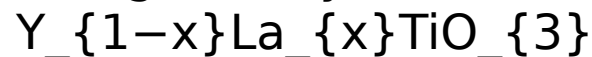


This is the accepted manuscript made available via CHORUS. The article has been published as:

## Lattice and magnetic dynamics in perovskite



Bing Li, Despina Louca, Jennifer Niedziela, Zongyao Li, Libin Zhang, Jianshi Zhou, and  
John B. Goodenough

Phys. Rev. B **94**, 224301 — Published 7 December 2016

DOI: [10.1103/PhysRevB.94.224301](https://doi.org/10.1103/PhysRevB.94.224301)

# An investigation of the lattice and magnetic dynamics in perovskite $\text{Y}_{1-x}\text{La}_x\text{TiO}_3$

Bing Li,<sup>1</sup> Despina Louca,<sup>1,\*</sup> Jennifer Niedziela,<sup>2</sup> and Zongyao Li<sup>3</sup>, Libin Zhang<sup>3</sup>, Jianshi Zhou<sup>3</sup>, John B. Goodenough<sup>3</sup>

<sup>1</sup>*Department of Physics, University of Virginia, Charlottesville, VA 22904, USA*

<sup>2</sup>*Spallation Neutron Source, Oak Ridge National Laboratory, Oak Ridge, TN 37831*

<sup>3</sup>*Materials Science and Engineering Program, Mechanical Engineering,  
University of Texas at Austin, Austin, TX 78712*

(Dated: November 18, 2016)

Inelastic neutron scattering combined with the dynamic pair density function (DPDF) analysis were used to investigate the magnetic and lattice dynamics in the orbitally active  $\text{Y}_{1-x}\text{La}_x\text{TiO}_3$  as it crosses the antiferromagnetic (AFM) to ferromagnetic (FM) phase boundary. Upon doping, the FM state present in  $\text{YTiO}_3$  is suppressed on approaching a critical concentration of  $x_c \sim 0.3$  in which  $T_C \simeq 0$ , and is replaced by the AFM phase of  $\text{LaTiO}_3$ . Below  $x_c$ , magnetic scattering from spin waves is dominant at low energies. At  $x_c$  with a  $T_C \simeq 0$ , magnetic scattering is also observed and is most likely due to AFM fluctuations. At the same time, local atomic fluctuations extending to 50 meV are observed above and below the magnetic transitions from  $0 \leq x \leq 1$  that show distinct characteristics with  $x$ . From Y to La, a clear difference is observed in the phonon density of states (DOS) as a function of doping as well. At  $x = 0.15$  and  $0.3$ , low energy modes involving predominantly the rare-earth ion become suppressed with increasing temperature while in  $x = 1$ , strong suppression of phonon modes across a wide range in energy is observed above  $T_N$ . It is likely that in the Y heavy samples, phonon modes below 20 meV have a stronger influence on the orbital excitations, while in  $\text{LaTiO}_3$ , a strong phonon dependence is observed upon cooling up to  $T_N$ .

PACS numbers: 61.05.F-, 61.66.Fn, 75.20.-g

## I. INTRODUCTION

Transition metal oxides are a fascinating class of materials that have captivated the research community for many decades. Their intricate magnetic and electronic properties stem from strong interactions among the charge, spin, lattice and orbital degrees of freedom. Many examples can be found in the literature that clearly demonstrate how strong coupling among the different degrees of freedom can lead to static and dynamic phase separation<sup>1</sup>, orbital ordering<sup>2-4</sup>, charge and spin stripes<sup>5</sup>, polaron localization<sup>6</sup>, and Jahn-Teller (JT) distortions<sup>7</sup>. Cooperative JT effects in  $e_g$ -orbitally active systems can elicit significant lattice distortions due to direct  $2p - 3d$  orbital overlap such as in the classic example of  $\text{LaMnO}_3$ <sup>8</sup>.

Of particular interest is the nature of the orbital-spin coupling in the  $t_{2g}$ -orbitally active titanates ( $\text{Ti}^{3+}$ ,  $3d^1$ ,  $S=\frac{1}{2}$ )<sup>9</sup>. The Mott insulating  $\text{RTiO}_3$  ( $R$ =rare-earth ion) perovskite is a model system by which one can study superexchange interactions in the paramagnetic phase where the orbital degree of freedom is released, as well as the crossover from AFM to FM exchange interactions as a function of the tolerance factor<sup>10-14</sup>. When  $R = \text{La}^{3+}$  as in  $\text{LaTiO}_3$ , a G-type AFM transition occurs at  $T_N = 140$  K. Decreasing the tolerance factor leads to a transition from the AFM to an FM state as in  $\text{Y}_{1-x}\text{La}_x\text{TiO}_3$ <sup>15,16</sup>. In  $\text{YTiO}_3$ , the FM transition temperature is observed at  $T_C \sim 30$  K. Coupled with this crossover are steric effects involving octahedral tilts and rotations that have a direct influence on the degree of orbital overlap and subsequently on the spin-spin interactions in titanates.

An important parameter is the Ti-O-Ti bond angle that bends from  $180^\circ$  with decreasing the  $R^{3+}$  nominal radius, leading to a reduction of the bandwidth,  $W$ . This leads to stronger electron correlations in  $\text{YTiO}_3$  because of the enhanced on-site Coulomb energy,  $U$ , than in  $\text{LaTiO}_3$ <sup>17-19</sup>.

Long-range orbital order has long been presumed to be a prerequisite for long-range magnetic order<sup>20</sup>. However, this is not clear in the case of  $\text{Y}_{1-x}\text{La}_x\text{TiO}_3$ . In a related compound,  $\text{YVO}_3$  ( $3d^2$ ) a transition to a G-type orbital order (G-OO) occurs at  $T_{OO} \sim 200$  K, followed by a C-type AFM spin order at  $T_N \sim 116$  K (C-SO) and finally to an orbital flip transition at  $T_{CG} \sim 77$  K with C-type orbital order (C-OO) and G-type spin order (G-SO)<sup>21-23</sup>. Moreover, these transitions are coupled to structural ones. Above 200 K and below 77 K, the crystal symmetry is orthorhombic, while in the  $77 \text{ K} < T < 200 \text{ K}$  range, the symmetry is monoclinic<sup>24</sup>. On the other end, in  $\text{LaVO}_3$ , the  $T_{OO}$  transition is suppressed, while the AFM transition at  $T_N \sim 143$  K is followed by a structural transition at  $T_t \sim 140$  K from the orthorhombic to the monoclinic phase, the latter of which accommodates a G-OO/C-SO phase<sup>25</sup>. In  $\text{RTiO}_3$  from La to Lu however, orbitals are disordered at temperatures above  $T > T_N$  where an orbital liquid state has been proposed to exist<sup>14</sup> in which state orbitals can potentially exhibit strong fluctuations. The substitution of Y for La introduces orbital fluctuations in the paramagnetic (PM) phase that create FM interactions that lead to the reduction of  $T_N$ . At a critical concentration of  $x_c \sim 0.3$ , the prevailing orbital fluctuations favor FM interactions below  $T_C$ . It is therefore assumed that the site distortions that favor orbital fluctuations change the magnetic order from FM in  $\text{YTiO}_3$  to AFM in  $\text{LaTiO}_3$ .

It is conceivable that orbital fluctuations are biased by intrinsic octahedral distortions of the orthorhombic perovskite lattice. However, static distortions of the  $\text{TiO}_6$  octahedra across the phase diagram have remained undetected by conventional diffraction measurements<sup>10,11</sup>. At the same time, it is quite possible that the local distortions are different from  $R=Y$  to  $La$ . Hence a real space analysis of the local structure using the pair density function technique is better suited to investigate the nature of site distortions that may favor orbital fluctuations that change magnetic exchange interactions.

To this end, elucidating the dynamic characteristics of the structural distortions associated with orbital fluctuations as a function of doping will help explain how one type of magnetic coupling is favored over the other depending on the local environment. The solid solution of  $\text{Y}_{1-x}\text{La}_x\text{TiO}_3$  contains no rare-earth moments and the  $\text{Ti}^{3+}$  in its  $t_{2g}^1$  configuration has a moment less than  $1\mu_B$  that is ideally expected for  $\text{Ti}^{3+}$  at the spin-only limit<sup>12-14</sup>. With increasing  $x$ , it is conceivable that local distortions introduced by the substitution confine the orbital fluctuations in such a way that they control the magnetic coupling, and may explain the AFM to FM transition. To characterize the local site distortions brought upon by doping, inelastic neutron scattering is used to determine the local fluctuations via the DPDF method. The DPDF, a Fourier transform of the dynamic structure function,  $S(Q, \omega)$ , is a measure of the local fluctuations of atomic pair correlations projected in real space that are not manifested via regular phonons. It is obtained using a high energy transfer,  $E_i$ , that allows for a large momentum transfer needed for the real space analysis. The  $S(Q, \omega)$  is also determined at lower energy transfers to illustrate how the magnetic and phonon excitations change across the critical concentration.

## II. EXPERIMENT

### A. Sample synthesis

Polycrystalline  $\text{LaTiO}_3$  was prepared by arc melting. The stoichiometric mixture of  $\text{La}_2\text{O}_3$ ,  $\text{Ti}_2\text{O}_3$  and  $\text{Ti}$ , with a  $\text{Ti}_2\text{O}_3$  to  $\text{Ti}$  metal molar ratio of 9:1, was ground and pressed into pellets 20 mm in diameter. The  $\text{La}_2\text{O}_3$  was heated to 1000 °C in air before weighing. The pellets were transferred quickly to the arc furnace to minimize absorption of moisture. The melted pellets were inverted and re-melted several times to improve homogeneity. The  $\text{Y}_{1-x}\text{La}_x\text{TiO}_3$  (with  $x = 0.15$  and  $0.3$ ) powders were synthesized by ball milling followed by spark plasma sintering (SPS). The starting materials,  $\text{Y}_2\text{O}_3$ ,  $\text{La}_2\text{O}_3$ ,  $\text{Ti}_2\text{O}_3$ , and  $\text{Ti}$  powders were weighed in the molar ratio of  $(1-x) : x : 0.9 : 0.2$ , and well mixed in an agate mortar. The powder mixture was then sealed in a tungsten carbide ball-milling jar under an argon atmosphere and ball milled for 60 minutes by using a SPEX 8000M Mixer/Mill. Next, the ball-milled powder was loaded in

a graphite die and sintered by SPS at 1600 °C for 10 minutes under 60 MPa. During the SPS process, the temperature was first kept at 1000 °C for 3 minutes and then increased to 1600 °C at a ramping rate of 60 °C/min. The hard pellet obtained after SPS was polished with sand paper in order to remove the surface layer of graphite and then ground into fine powder. Powder x-ray diffraction was performed to check that the samples were single phase and the oxygen stoichiometry was verified by a thermoelectric power measurement.

### B. Neutron measurements and analysis

The inelastic neutron scattering experiments were carried out at the wide Angular-Range Chopper Spectrometer (ARCS) at the Spallation Neutron Source of Oak Ridge National Laboratory. Four different incident energies were used:  $E_i = 20, 30, 80$  and  $320$  meV. Data were collected at 5, 50 and 150 K. The data collected at lower energies were used to investigate the doping dependence of the magnetic excitations. The medium energy data of 80 meV was used to obtain the generalized phonon density of states (GDOS) while the 320 meV data was used to determine the DPDF, the analysis of which is discussed next. The background contributions from the cryostat and sample container were subtracted from the data. The measured intensity was normalized by that of vanadium measured in the same conditions.

The inelastic spectrum is comprised of the elastic line centered at  $E = 0$  that contains all the Bragg scattering and is the most intense. Away from the elastic line, the intensity becomes much weaker. The fitting of the elastic line of the data collected at an  $E_i = 320$  meV by a Gaussian function yields a full-width-half-max of  $\sim 12$  meV. To calculate the energy dependent PDF, the dynamic structure function,  $S(Q, \omega)$ , is integrated in a series of energy cuts with a constant energy window of  $\pm 7$  meV. The powder averaging process and the high incoming energy make the  $S(Q, \omega)$  quite featureless. The highest momentum transfer reached was  $Q_{max} \sim 22 \text{ \AA}^{-1}$ .

Multiple and incoherent scattering corrections are also implemented in the analysis. These have slow  $Q$ - and  $E$ -dependent contributions to the scattering intensity, and are defined as follows:

$$B(Q, \omega) = A + BQ^2 \exp(Q^2 \langle u^2 \rangle / 3) \quad (1)$$

in the case of small  $\langle u \rangle$ , the atomic displacements away from the equilibrium site. The form of  $B(Q, \omega)$  was selected such that constants  $A$ ,  $B$  and  $\langle u^2 \rangle$  were obtained by fitting the non-oscillatory contribution to  $S_d(Q, \omega)$  at each energy integration, where  $S_d(Q, \omega)$  is an energy-limited function relating the nature of the dynamics associated over the selected energy range<sup>26,27</sup>. The constant  $A$  takes into account a flat multiple scattering contribution and the exponential term corresponds to the Debye-Waller factor representing the vibrational motion of the

atoms. The distinct inelastic  $I_d(Q, \omega)$  function is defined as

$$I_d(Q, \omega) = S_d(Q, \omega) - B(Q, \omega). \quad (2)$$

The  $I_d(Q, \omega)$  is Fourier transformed to obtain the dynamic PDF:

$$\rho_d(r, \omega) = \rho_0 + \frac{1}{2\pi^2 r} \int Q_d I_d(Q, \omega) \sin(Qr) dQ \quad (3)$$

Based on the energy cuts of  $I_d(Q, \omega)$ , a series of snapshot PDF's at the corresponding energy windows are obtained, which allows us to study the frequency dependence of the local atomic correlations. The DPDF is used to study the local lattice dynamics and the results are combined with the density of states obtained using the 80 meV data as they are quite complimentary, in order to understand the nature of the distortions with doping. Details of this technique can be found in Ref.<sup>28</sup>. The GDOS is calculated using the DAVE software<sup>29</sup>.

The spin wave simulations were performed using the SpinW code<sup>30</sup>. The spin Hamiltonian used in the calculation is as follows:

$$H = \sum_{i,j} J_{ij} S_i \cdot S_j + \sum_i A_i S_i \cdot S_i \quad (4)$$

where  $S_i$  are spin vector operators,  $J_{ij}$  is the exchange coupling between  $i$  and  $j$  spins, and  $A_i$  corresponds to the single ion anisotropy term associated with spin  $i$ . The spin wave spectrum for  $\text{YTiO}_3$  is calculated using an isotropic nearest neighbor coupling constant  $J = -2.75$  meV and a uniaxial anisotropy  $A = 0.8$  meV on a tetragonal lattice with  $a = b = 3.90$  Å, and  $c = 3.80$  Å. In  $\text{LaTiO}_3$ , a  $J = 15.5$  meV is used and a cubic lattice is assumed with  $a = 3.95$  Å. The value for  $J$  is obtained from the single crystal data of Ref.<sup>14</sup>. The results from these simulations are used to separate the magnetic from the phonon contributions in the dynamic structure function.

### III. RESULTS

#### A. Dynamics of the local structure

The crystal symmetry is orthorhombic in both  $\text{YTiO}_3$  and  $\text{LaTiO}_3$ , with the  $Pnma$  space group. A schematic of the unit cell is shown in Fig. 1(a). The  $\text{TiO}_{6/2}$  octahedra are deformed, leading to deviations from the cubic symmetry and splitting of the  $t_{2g}$  orbitals that may promote orbital ordering<sup>31-33</sup>, although such a state has not been observed. In  $\text{YTiO}_3$ , the octahedral distortions have been described to be of the JT-type, while in  $\text{LaTiO}_3$ , the distortions are of the  $\text{GdFeO}_3$ -type and with significant differences of the Ti-O-Ti bond angles. These differences may also explain their magnetic properties<sup>34-36</sup>. In Fig. 1(b), the correlation functions representing the

local atomic structures for  $\text{YTiO}_3$  and  $\text{LaTiO}_3$  are plotted. The model function is calculated using the lattice constants and unit cell parameters obtained from the crystallographic refinement of diffraction data. The first peak corresponds to the  $\text{TiO}_3$  octahedral pair bonds and it is the shortest in the crystal. Note that this peak is negative because Ti has a negative neutron scattering length and it is almost identical in both compounds. Following are the positive R-O and O-O pair correlation peaks. Differences are observed between the two compounds starting with the second peak and beyond that cannot be simply accounted for by replacing La for Y, and are instead explained by the octahedral distortions prevalent in the two systems. Also obtained from the model is the set of partial functions that will be useful in identifying specific contributions of atoms as a function of  $r$ .

To investigate the composition and temperature dependence of the dynamics associated with octahedral fluctuations, four compositions were measured from  $0 \leq x \leq 1$  and the results from the DPDF ( $\rho_d(r, \omega)$ ) analysis are summarized in Fig. 2. The data collected at two temperatures, 5 and 150 K, are shown in the upper and lower panels, respectively. The intensity plots for  $\text{Y}_{1-x}\text{La}_x\text{TiO}_3$  are shown in (a) for  $x = 0$ , in (b) for  $x = 0.15$ , in (c) for  $x = 0.30$  and in (d) for  $x = 1$ . The vertical axis corresponds to cuts in energy while the horizontal axis is distance in real space. The analysis for the  $x = 0$  composition was previously reported in Ref.<sup>28</sup> and it is included here for comparison. As a function of energy, the DPDF is extended up to 50 meV, where the most intense peaks appear below  $\sim 5$  Å. The Ti-O octahedral pairs correspond to the first blue bar in the plots. The DPDF intensity for the Ti-O bonds extends to 50 meV indicating that the Ti-O correlations are fluctuating at least up to this energy. Beyond this energy, the intensity gets very weak. As a function of increasing  $x$ , the Ti-O local fluctuations weaken, and the intensity bar becomes narrower with doping above 20 meV, unlike in  $\text{YTiO}_3$ . Furthermore, in the DPDF of  $x = 0$  shown in Figs. 2(a) and (e)), a split is observed at the Y-O bonds  $\sim 2.25$  Å above 40 meV. Even though this peak shifts to the right upon doping, it is clear that the split is absent in  $x = 0.15, 0.3$  and  $1.0$ . This suggests that the La substitution suppresses the split even though the correlations are extended in the same energy range. At longer distances, further compositional dependence is observed that reflects the changing dynamics with doping. It is evident that the correlations  $\sim 3.5$  Å due to O-O, R-O and R-Ti pairs show a clear split with doping around 30 meV and above. This becomes quite clear with increasing doping as can be seen in the 5 K data of the  $x = 0.3$  and  $1.0$  where the split sets in at  $\sim 25$  meV. Similar changes are observed at 4 Å and beyond as a function of doping.

The dynamic changes shown here signal the presence of local atomic fluctuations that vary as a function of doping. Can these local fluctuations lift the orbital de-

generacy? The DPDFs of the lower panels collected at 150 K, in the orbitally disordered state, show some differences from the DPDFs of the upper panels at 5 K except in  $\text{LaTiO}_3$ . A comparison of Figs. 2(d) and 2(h) shows little change upon cooling that may indicate that the same orbital fluctuations present at high temperatures persist down to low temperatures. However, in the panels corresponding to  $x = 0, 0.15$  and  $0.3$ , a temperature dependence is observed. This suggests that the local atomic fluctuations involving R-O and R-Ti and second nearest Ti-O pairs are changing that may be in response to orbital fluctuations.

## B. Magnetic and Phonon Excitations

Three different incident energies,  $E_i = 20, 30$  and  $80$  meV, were used to explore the magnetic and phonon excitations as a function of doping and temperature. Starting with the ferromagnetic  $x = 0.15$  composition with a  $T_C$  of  $20$  K, in the  $E_i = 20$  meV contour plot of energy ( $E$ ) versus momentum transfer ( $Q$ ) shown in Fig. 3(a), a very low energy excitation below  $10$  meV is observed that is magnetic in nature as will be shown by the simulated magnon spectrum below. At  $T_C$ , the low energy excitation shrinks but a broader in energy intensity is observed which is shown in the intensity plot of  $S(Q, \omega)$  in Fig. 3(b) that is a cut across  $Q$  from  $0.5$  to  $2.5 \text{ \AA}^{-1}$ .

Continuing on with the  $x = 0.3$  composition that resides at the cross-over between the FM and the AFM transition in the  $\text{Y}_{1-x}\text{La}_x\text{TiO}_3$  phase diagram, similar excitations are observed as in the  $x = 0.15$ . In particular, low energy excitations clearly visible with the  $E_i = 20$  meV are present just as in the  $50$  K data of the  $x = 0.15$  sample (Fig. 3(c)). Note that at  $x = 0.3$ ,  $T_C = 0$ . Hence the low energy excitations cannot arise from the magnon dispersion. These excitations are however much stronger in the  $x = 0.3$  as a function of increasing temperature as seen in Fig. 3(d) suggesting that the magnetic fluctuations are stronger in the  $x = 0.3$ . At  $E_i = 30$  meV, the low energy magnetic excitations are equally pronounced. At the same time, more phonon excitations become evident. Several excitations are observed that spread across in energy and increase in intensity with increasing  $Q$ .

At  $E_i = 80$  meV, the phonon contribution dominates the spectrum. This is used to determine the GDOS for the  $x = 0.15$  and  $x = 0.3$  samples. The results are plotted in Fig. 4. Overall the GDOS between the  $x = 0.15$  and  $0.30$  look similar, however some small differences are observed in the temperature dependence of the GDOS function of the two sample that signals differences in their active phonon modes, especially below  $20$  meV. These low-energy excitations most likely involve R-O and Ti-O modes.

The G-type AFM  $\text{LaTiO}_3$  end member has a very different spectrum as can be seen from the results that are summarized in Fig. 5. The E-Q contour plot is shown for data collected using an  $E_i = 80$  meV at  $5$  K (Fig.

5(a)). Several excitations are observed at high energies that exhibit a strong temperature dependence. However, the low energy excitation observed in the  $x = 0.15$  and  $0.3$  is much weaker in the  $\text{LaTiO}_3$ . In  $\text{LaTiO}_3$ , a strong (101) magnetic peak is located at  $Q = 1.46 \text{ \AA}^{-1}$ . The magnetic excitations observed in the  $x = 0.15$  and  $0.30$  may have their origin to the AFM exchange interactions in  $\text{LaTiO}_3$ .

The temperature dependence of the GDOS is shown in Fig. 5 (b) which is a plot for data collected from  $5$  to  $250$  K. Little to no temperature dependence is observed up to  $100$  K. However, between  $100$  and  $150$  K, a most striking change is observed with the suppression of the intensity around  $40$  meV that involves O and Ti modes. This temperature is very close to the AFM transition. Around  $50$  meV, the shape of the GDOS spectrum changes as well. With increasing the temperature further, at  $200$  K, additional changes become apparent in the GDOS at around  $10$  and  $25$  meV, that involve rare-earth and Ti modes. Previous Raman measurements showed that higher frequency modes, above  $80$  meV, softened below  $T_N$  due to a structural rearrangement<sup>37</sup>. Here, changes are observed even above  $T_N$  that indicate that the specific phonon modes are actively involved in selecting the magnetic state. In comparison to the GDOS for  $x = 0.15$  and  $0.30$  shown in Fig. 4, where only low energy modes show some temperature dependence with the intensity becoming suppressed with increasing temperature, it becomes evident that above the critical concentration, different phonon modes become active in  $\text{LaTiO}_3$ .

The powder averaged magnon spectrum is calculated and the results are shown in Figs. 6(a) and 6(b) for  $\text{YTiO}_3$  and  $\text{LaTiO}_3$ , respectively. Only nearest neighbor exchange interactions are taken in account and an energy anisotropy is included in the calculation of  $\text{YTiO}_3$ . In  $\text{YTiO}_3$ , the dispersion shows the most intensity below  $12$  meV in energy and  $2 \text{ \AA}^{-1}$  in  $Q$ , in agreement with the data shown in Fig. 3 (a) for the FM  $x = 0.15$ . A coupling constant,  $J$ , of  $2.75$  meV is obtained which is in agreement with Refs.<sup>13,14</sup>. In  $\text{LaTiO}_3$ , the magnon dispersion reaches a maximum below  $50$  meV and the exchange constant is estimated to be  $15.5$  meV. Even though no low energy transfer data were collected for  $\text{LaTiO}_3$ , one can see from Fig. 5(a) that intensity grows from the position of the magnetic Bragg peaks. The very high energy of the magnon spectrum overlaps with the phonon spectrum but the strong  $Q$ -dependence of the phonon dominates the GDOS.

## IV. SUMMARY

The magnetic and lattice dynamics were investigated in  $\text{Y}_{1-x}\text{La}_x\text{TiO}_3$  using inelastic neutron scattering and the DPDF analysis. The DPDF provides a description of the fluctuating in energy local correlations, while contributions from regular phonons lead to broadening of the DPDF peaks. The DPDF captures the fluctuating mo-

tion arising from modes contributing to the flat part of the phonon dispersion involving optical branches<sup>38</sup>. In the FM titanates below  $x_c = 0.3$ , Ti-O and R-O fluctuations persist to high energies. The frequency dependence of the Y/La-O, Ti-O and O-O local correlations as a function of doping indicates that the local modes associated with these correlations are strongly anharmonic. Below 25 meV, it can be seen that the fluctuations vary in time but are well positioned in real space. Above 25 meV, the central R-O peak is split to two, most likely because the R and O atoms are connected via a double-well potential where the bond length between the two atoms can oscillate. With increasing temperature, the intensity of the DPDF peaks is not diminished indicating that atomic fluctuations persist. Overall, the DPDF intensity above 25 meV is strongly localized to the Ti-O, R-O and O-O nearest neighbors.

Magnetic scattering very close to the elastic line is observed in the  $x = 0.15$  above and below  $T_C$  that arises from the powder averaged magnon dispersion. By increasing the doping to  $x = 0.30$ , even though no magnetic transition is present, it is possible that magnetic fluctuations are still present intensity plot of  $S(Q, \omega)$  in Fig. 3(b) that is a cut across  $Q$  from 0.5 to 2.5  $\text{\AA}^{-1}$ . At the same time, the most temperature dependent changes observed from the GDOS measurements are from about 20 meV and below. Similarly to the GDOS of the  $x = 0.15$ , a temperature dependence is observed in the  $x = 0.30$  as well below 20 meV. These phonon modes most likely involve the rare-earth ion and is most likely related to the enhanced tilting of the  $\text{TiO}_6$  octahedra. On the

other end, a wider in energy temperature dependence is observed in the GDOS of  $\text{LaTiO}_3$ , indicating that the AFM transition is coupled to not only  $\text{TiO}_6$  tilting but to O-O and Ti-O phonon mode fluctuations.

In the  $\text{GdFeO}_3$ -type distorted  $\text{RTiO}_3$  system, as the  $\text{R}^{3+}$  ion gets smaller and the structural distortion is enhanced, a crossover from an AFM, orbital liquid ( $\text{LaTiO}_3$ ) to an FM antiferro-orbital ordering ( $\text{YTiO}_3$ ) state has been suggested to occur<sup>16,39</sup>. It has been shown that the bond angle Ti-O-Ti, plays an important role in determining the ground state of magnetism and orbital order.<sup>9</sup> According to theoretical calculations<sup>40</sup>, the FM phase, stabilized by enhanced tilting, favors the presence of antiferro-orbital ordering. Thus, the atomic fluctuations described above must exert some influence on the orbital state of Ti. From  $\text{YTiO}_3$  to  $\text{LaTiO}_3$ , the localized fluctuations change in nature that are linked to the different  $\text{GeFeO}_3$ -type distortions i.e. tilt angle, present in both systems<sup>9</sup>. Moreover, the GDOS results clearly show that different phonon modes are thermally active in the AFM and FM ends of the phase diagram.

## Acknowledgments

This work has been supported by the Department of Energy, Grant number DE-FG02-01ER45927 and the National Science Foundation, Grant number DMR1122603 and Major Research Instrument Grant number DMR-1229131.

---

\* Electronic address: louca@virginia.edu

<sup>1</sup> E. Dagotto, *Science* **309**, 257 (2005).

<sup>2</sup> M. Imada, A. Fujimori, and Y. Tokura, *Rev. Mod. Phys.* **70**, (1998).

<sup>3</sup> Y. Tokura and N. Nagaosa, *Science* **288**, 462 (2000).

<sup>4</sup> D. I. Khomskii, *Phys. Scripta* **72**, CC8 (2005).

<sup>5</sup> J. M. Tranquada, B. J. Sternlieb, J. D. Axe, Y. Nakamura, and S. Uchida, *Nature* **375**, 561 (1995).

<sup>6</sup> D. Louca, T. Egami, E. L. Brosha, H. Röder and A. R. Bishop, *Phys. Rev. B* **56**, R8475 (1997).

<sup>7</sup> K. I. Kugel and D. I. Khomskii, *Zh. Eksp. Teor. Fiz.* **64**, 1429 (1973) [*Sov. Phys. JETP* **37**, 725 (1973)].

<sup>8</sup> F. Moussa, M. Hennion, J. Rodriguez-Carvajal, H. Moudén, L. Pinsard, and A. Revcolevschi, *Phys. Rev. B* **54**, 15149 (1996).

<sup>9</sup> M. Mochizuki and M. Imada, *New J. Phys.* **6**, 154 (2004).

<sup>10</sup> D. A. MacLean, H.-N. Ng, and J. E. Greedan, *J. Solid State Chem.* **30**, 35 (1979).

<sup>11</sup> M. Eitel and J. E. Greedan, *J. Less Common Met.* **116**, 95 (1986).

<sup>12</sup> A. C. Komarek, H. Roth, M. Cwik, W.-D. Stein, J. Baier, M. Kriener, F. Bourae, T. Lorenz, and M. Braden, *Phys. Rev. B* **75**, 224402 (2007).

<sup>13</sup> C. Ulrich, G. Khaliullin, S. Okamoto, M. Reehuis, A. Ivanov, H. He, Y. Taguchi, Y. Tokura, and B. Keimer,

*Phys. Rev. Lett.* **89**, 167202 (2002).

<sup>14</sup> B. Keimer, D. Casa, A. Ivanov, J. W. Lynn, M. v. Zimmermann, J. P. Hill, D. Gibbs, Y. Taguchi, and Y. Tokura, *Phys. Rev. Lett.* **85**, 3946 (2000).

<sup>15</sup> H. D. Zhou and J. B. Goodenough, *J. Phys.: Condens. Matter* **17**, 7395 (2005).

<sup>16</sup> J. G. Cheng, Y. Sui, J. S. Zhou, J. B. Goodenough, and W. H. Su, *Phys. Rev. Lett.* **101**, 087205 (2008).

<sup>17</sup> T. Mizokawa, D. I. Khomskii, and G. A. Sawatzky, *Phys. Rev. B* **60**, 7309 (1999).

<sup>18</sup> G. Khaliullin and S. Okamoto, *Phys. Rev. B* **68**, 205109 (2003).

<sup>19</sup> Y. Furukawa, I. Okamura, K. Kumagai, Y. Taguchi, and Y. Tokura, *Physica B: Cond. Matt.* **237-238**, 39 (1997).

<sup>20</sup> L. Paolasini, R. Caciuffo, A. Sollier, P. Ghigna, and M. Altarelli, *Phys. Rev. Lett.* **88**, 106403 (2002); R. Caciuffo, L. Paolasini, A. Sollier, P. Ghigna, E. Pavarini, J. van den Brink, and M. Altarelli, *Phys. Rev. B* **65**, 174425 (2002).

<sup>21</sup> K. Kawano, H. Yoshizawa, and Y. Ueda, *J. Phys. Soc. Jpn.* **63**, 2857 (1994).

<sup>22</sup> C. Ulrich, G. Khaliullin, J. Sirker, M. Reehuis, M. Ohl, S. Miyasaka, Y. Tokura, and B. Keimer, *Phys. Rev. Lett.* **91**, 257202 (2003).

<sup>23</sup> S. Yano, D. Louca, J. C. Neuefeind, J.-Q. Yan, J.-S. Zhou, and J. B. Goodenough, *Phys. Rev. B* **90**, 214111 (2014).

- <sup>24</sup> G. R. Blake, T. T. M. Palstra, Y. Ren, A. A. Nughoho, and A. A. Menovsky, Phys. Rev. Lett. **87**, 245501 (2001); Phys. Rev. B **65**, 174112 (2002).
- <sup>25</sup> P. Bordet, C. Chaillout, M. Marezio, Q. Huang, A. Santoro, S.-W. Cheong, H. Takagi, C. S. Oglesby, and B. Batlogg, J. Solid. State. Chem. **106**, 253 (1993).
- <sup>26</sup> A. C. Hannon, M. Arai, and R. G. Delaplane, Nucl. Inst. Meth. Phys. Res. A **354**, 96 (1995).
- <sup>27</sup> A. C. Hannon, M. Arai, R. N. Sinclair, and A. C. Wright, J. Non-Cryst. Solids **150**, 239 (1992).
- <sup>28</sup> B. Li, D. Louca, B. Hu, J. L. Niedziela, J. Zhou, and J. B. Goodenough, J. Phys. Soc. Jpn. **83**, 084601 (2014).
- <sup>29</sup> R.T. Azuah, L.R. Kneller, Y. Qiu, P.L.W. Tregenna-Piggott, C.M. Brown, J.R.D. Copley, and R.M. Dimeo, J. Res. Natl. Inst. Stan. Technol. **114**, 341 (2009).
- <sup>30</sup> S. Toth and B. Lake, J. Phys.: Condens. Matter **27**, 166002 (2015).
- <sup>31</sup> H. Ichikawa, J. Akimitsu, M. Nishi, and K. Kakurai, Physica B **281&282**, 482 (2000).
- <sup>32</sup> J. Akimitsu, H. Ichikawa, N. Eguchi, T. Miyano, M. Nishi and K. Kakurai, J. Phys. Soc. Jpn. **70**, 3475 (2001).
- <sup>33</sup> T. Kiyama and I. Masayuki, Phys. Rev. Lett. **91**, 167202 (2003). T. Kiyama, H. Saitoh, M. Itoh, K. Kodama, H. Ichikawa, and J. Akimitsu, J. Phys. Soc. Jpn. **74**, 1123 (2005).
- <sup>34</sup> I. V. Solovyev, Phys. Rev. B **69**, 134403 (2004).
- <sup>35</sup> M. Cwik, T. Lorenz, J. Baier, R. Müller, G. André, F. Bourée, F. Lichtenberg, A. Freimuth, R. Schmitz, E. Müller-Hartmann, and M. Braden, Phys. Rev. B **68**, 060401(R) (2003).
- <sup>36</sup> M. Mochizuki and M. Imada, J. Phys. Soc. Jpn. **73**, 1833 (2004); Phys. Rev. Lett. **91**, 167203 (2003).
- <sup>37</sup> M. N. Iliev, A. P. Litvinchuk, M. V. Abrashev, V. N. Popov, J. Cmaidalka, B. Lorenz, and R. L. Meng, Phys. Rev. B **69**, 172301 (2004).
- <sup>38</sup> W. Dmowski, S. B. Vakhrushev, I.-K. Jeong, M. P. Hehlen, F. Trouw, and T. Egami, Phys. Rev. Lett. **100**, 137602 (2008).
- <sup>39</sup> G. Khaliullin and S. Maekawa, Phys. Rev. Lett. **85**, 3950 (2000).
- <sup>40</sup> G. Khaliullin and S. Okamoto, Phys. Rev. Lett. **89**, 167201 (2002).

Figure Captions

FIG. 1: (a) The *Pnma* unit cell. (b) Two model PDFs corresponding to the local atomic structures of  $\text{YTiO}_3$  and  $\text{LaTiO}_3$  are calculated based on the average symmetry. The first peak corresponds to the Ti-O bonds. The observed differences are due to the different octahedral distortions. In (b), the partial functions for select pairs are shown.

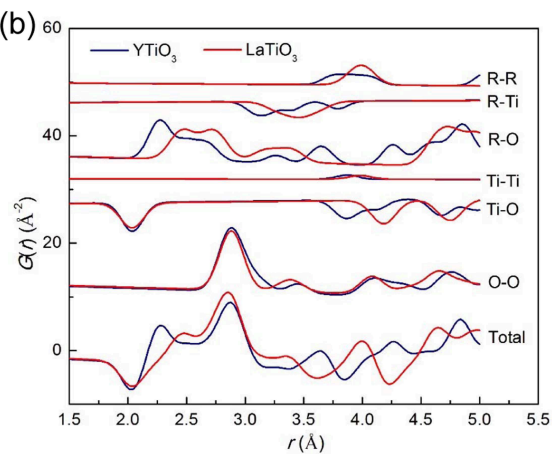
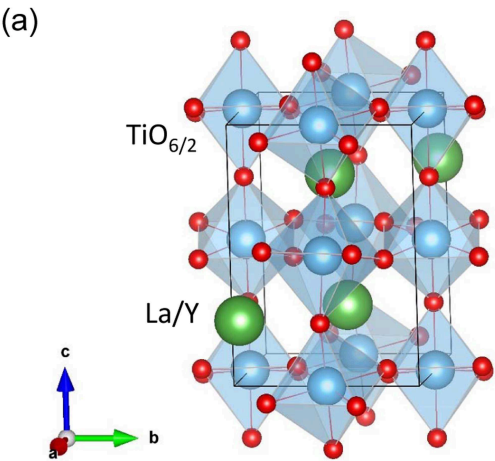
FIG. 2: (a)-(h) The DPDFs for  $x = 0, 0.15, 0.30$  and 1 at 5 and 150 K are plotted at the same intensity scale. The DPDFs were determined using the  $E_i = 320$  meV data.

FIG. 3: The E-Q contour map for  $x = 0.15$  at  $E_i = 20$  (a) and cuts in the low Q range in (b) are shown. Similarly, the contour maps and related constant Q cuts are shown in (c) and (d) for  $x = 0.30$ . The contour plots are from data collected at 5 K.

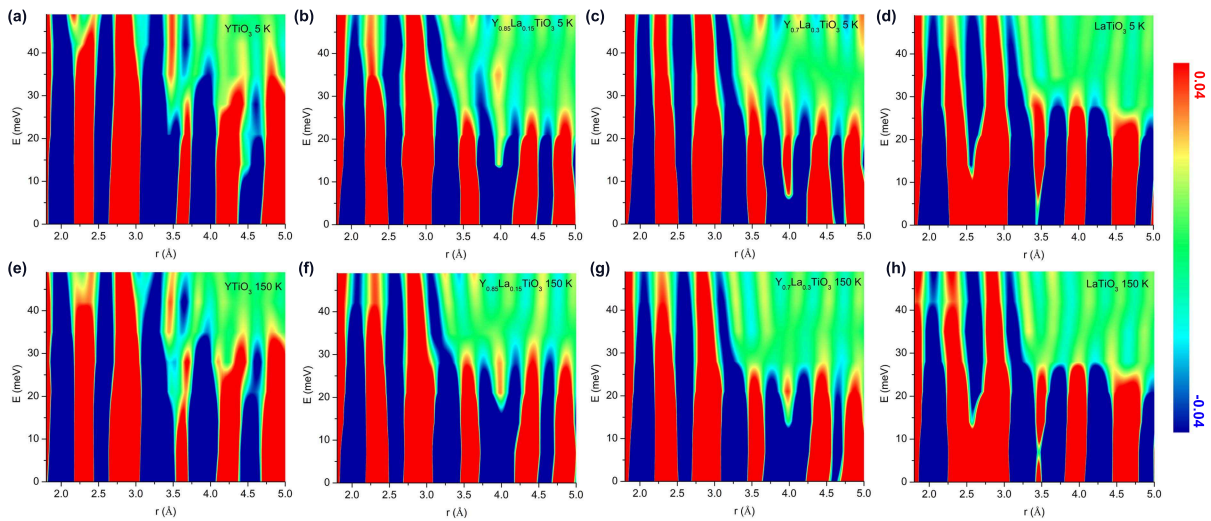
FIG. 4: The GDOS for  $x = 0.15$  (a) and  $x = 0.30$  (b) using the  $E_i = 80$  meV data are plotted as a function of temperature. Only the low energy phonon modes involving the rare-earth and possibly Ti ions are suppressed upon warming.

FIG. 5: In (a), the E-Q contour map is shown for the powder sample of  $\text{LaTiO}_3$  at 5 K using an incident energy of  $E_i = 80$  meV. Several phonon modes are evident at high Q, while at lower Q, the magnetic intensity appears much weaker. In (b), the GDOS is calculated using the  $E_i = 80$  meV data as a function of temperature. Upon warming, a clear suppression of the intensity of the phonon modes around 40 meV is observed between 100 and 150 K, in the temperature range of the magnetic transition, providing direct evidence for the phonon to magnetic coupling. These modes most likely involve the  $\text{TiO}_3$  octahedra. Further changes are observed at 200 K and above, in the range of 25 meV and below, indicating the involvement of La modes. The temperature dependence at 200 K and above may signal structural changes well above the AFM transition.

FIG. 6: In (a), the calculated magnon dispersion for a powder sample of  $\text{YTiO}_3$  and (b)  $\text{LaTiO}_3$  are shown.







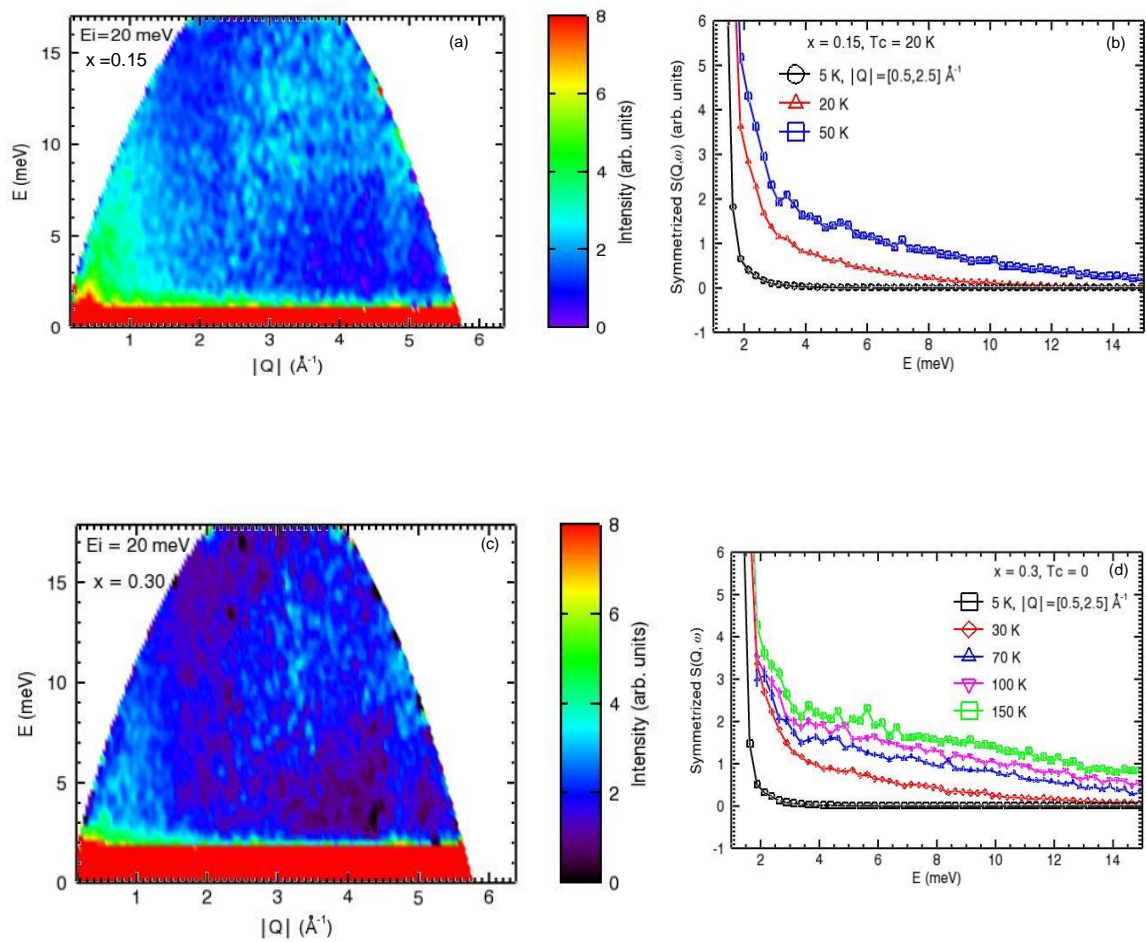


Fig. 3, Li et al

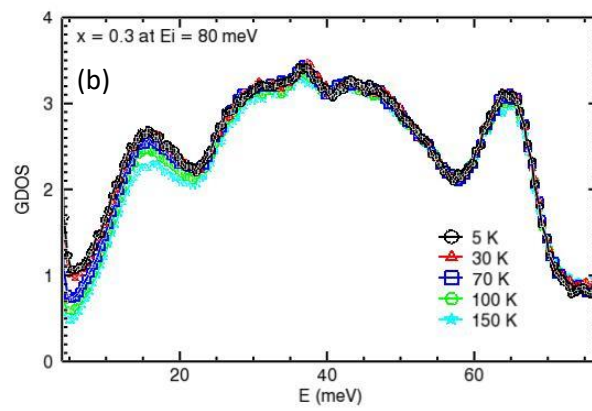
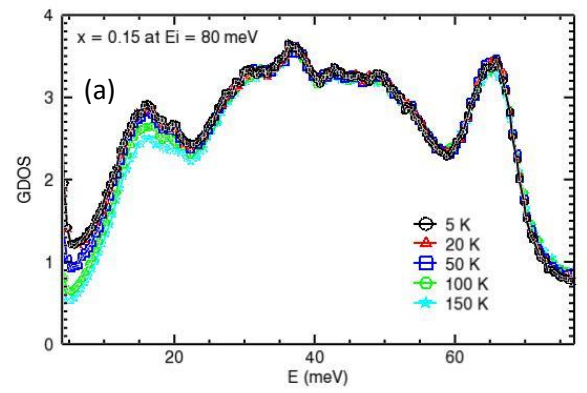


Fig. 4, Li et al

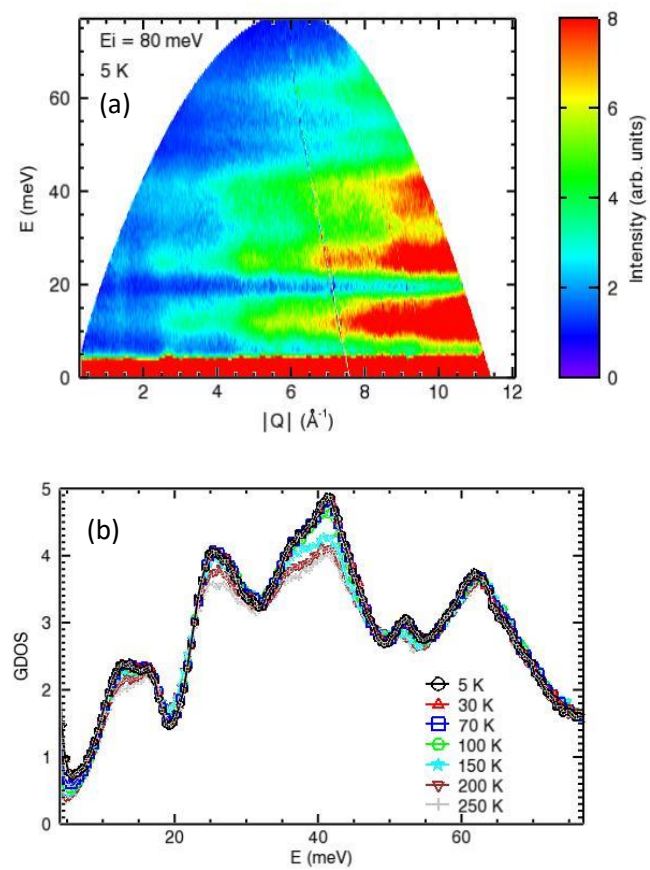


Fig. 5, Li et al

